J. Fluid Mech. (1993), *vol.* 256, *pp.* 133–161

Unsteady natural convection in a cavity with non-uniform absorption of radiation

By MICHAEL J. COATES AND JOHN C. PATTERSON
Department of Environmental Engineering *and* Centre for Water Research,
University of Western Australia, Nedlands, Western Australia

(Received 30 March 1992 and in revised form 3 March 1993)

A study of the unsteady natural convection in a cavity which was heated by the absorption of radiation entering through part of the surface is reported. While a general scaling analysis is quite complex, involving five separate timescales, most naturally occurring problems fall into just one regime, and it is only this regime which is discussed. To test the scaling, a series of laboratory experiments were performed in which the radiation parameters (surface flux and attenuation coefficient) were varied. The method by which these parameters were determined is also discussed. Numerical experiments were used to extend the parameter range, and the results of all these experiments confirmed the validity of the scaling over a range of parameters.

1. Introduction

In a recent review of physical limnology, Imberger & Patterson (1990) stressed the importance of turbidity patches within a lake or reservoir. These patches are usually areas in which there is an increase in the suspended particulate matter within the water. The suspended particles can be of both inanimate and animate origin, such as detrital material or phytoplankton, and are generally dark, making them good absorbers of the incoming radiation. Furthermore, the particles scatter light, which in turn increases the likelihood that the light will be absorbed. As the water itself is also generally coloured by dissolved pigments such as gilvin (Kirk 1983), which enhance the absorption, the overall result is that the light absorption in the turbid patches can be up to two orders of magnitude greater than in clear water (Kirk 1986) and as a consequence of this, the water temperature in the patches will be higher than that in the clear water.

A variation on the turbidity problem is to reduce the radiation flux entering at the water surface rather than altering how that radiation is absorbed within the water. This situation arises when there is a layer of opaque material on the water surface such as thick floating vegetation mats (Bowmaker 1976) or hyperscums (Zohary & Madeira 1990). In these problems, it is the open water heated by the full sun that has the higher temperature, and the temperature gradient establishes a flow from the open water into the shaded region which will alter the nutrient balance of the water beneath the plant layer. Thus the flow may have considerable importance to the biological activity beneath the plant layer.

The physics of the absorption process is complex (Viskanta & Toor 1978; Kirk 1983; Incropera, Craig & Houf 1984), but in the present context, which is directed at a parameterization of the resulting flow, a simple exponential absorption description is appropriate. This description is commonly used in limnology and oceanography.

The absorption of the radiation within the water column is one of a class of natural-convection problems driven by a distribution of internal heat sources. Internal source

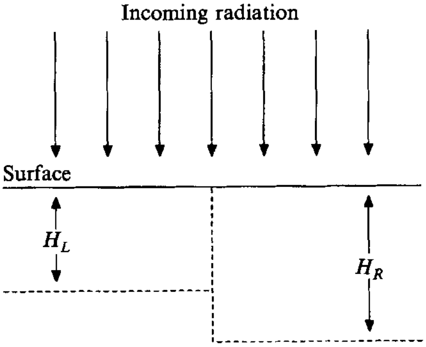

FIGURE 1. A sketch showing the situation considered by Trevisan & Bejan (1986). Each half is a semi-infinite region in which the incoming radiation is evenly absorbed down to some depth. The penetration depth has a different value in each half.

term problems in porous media have received considerable attention in the literature, owing to their importance in engineering applications such as the underground storage of radioactive waste or of freeze drying of foodstuffs. Typical of recent studies are those of Beckermann & Viskanta (1988), Chelliah & Viskanta (1989), and Islam & Nandakumar (1990).

Two models have been developed for unsteady natural convection with internal energy sources in fluid-filled cavities. Patterson (1984) derived a theoretical scaling analysis for a cavity in which the internal heat source varied longitudinally but was constant vertically and in time, and then verified some of the scaling regimes he found with numerical experiments. In the regime into which virtually all naturally occurring problems fall, Patterson found that at steady state there was a single gyre with horizontal isotherms (except at the boundaries), and the approach to steady state was oscillatory due to the presence of internal waves.

Trevisan & Bejan (1986, referred to as TB in the following), replaced Patterson's longitudinally varying internal heat source with one that was more representative of the absorption of radiation. In their model, the internal source term was the local heating generated by the absorption of radiation which entered the cavity through the surface. Nevertheless, their model of the radiative absorption was a very simple one. The cavity was divided into two horizontally semi-infinite regions, and in each of these it was assumed that the incoming energy flux entering through the surface was absorbed uniformly from the surface down to some specified depth (figure 1). That depth was different for the two regions. Immediately below these characteristic depths, there was no heating. Since these depths were different, but the total energy entering both halves was the same, the rate of temperature increase in the thinner region was larger as the energy was absorbed in a smaller volume. Consequently, a temperature gradient was established between the two regions, driving a circulation between them. A second circulation is expected in this problem since the cooler region has a greater depth than the hotter region. Thus there is a second temperature gradient between the cooler water on one side and the cold water immediately beneath the hot upper layer.

The scaling analysis of TB assumed that each region was semi-infinite, and therefore there was no horizontal lengthscale for the problem. As a result, the flow cannot be characterized by regimes delineated by a Grashof-number range as Patterson (1984) had done. Instead, the flow passed through five distinct regimes. These were (i) thermal diffusion in both, (ii) inertial upper and lower flows, (iii) viscous upper but inertial lower flow, (iv) viscous upper and lower flows, and finally (v) no flow as thermal diffusion penetrated the deeper layer. In their numerical simulations, TB simplified the problem by allowing the radiation to penetrate the full depth of the cavity in one side, and to a smaller depth in the other. The two gyres expected were found in their numerical simulations. TB were also able to find an analytical solution at very early times for the problem in which part of the water surface is shaded. That solution showed a single gyre as expected, since there was only one heated region. The temperature field was essentially that a conducting solid.

Radiation has an important effect on natural convection. For example, Fusegi & Farouk (1989) numerically investigated a square cavity in which the convection was driven by differentially heated endwalls. The cavity contained a gas with prescribed radiative properties. Their results showed that the simple gyres such as those predicted by Patterson & Imberger (1980) were established for simulations in which the gas did not radiate, but when radiating gases were used in the simulations, the gyres could be substantially distorted and even destroyed by the effects of the radiation.

In spite of the importance of radiation on natural convection, most studies of coupled radiation and convection have been oriented towards high-temperature gas flows in ducts and nozzles, such as in aircraft or rocket engines (for example, Soufiani & Taine 1987), and there is little work done on the convective effect of the absorption of solar radiation at normal temperatures. Webb & Viskanta (1987) investigated the flows generated by the absorption of radiation from the side in a small test cell with insulating upper and lower boundaries, and isothermal sidewalls. The source used a series of lamps to simulate the solar spectrum. Their results showed a large-scale circulation with a strong boundary layer on the transparent wall. Since water absorbs very strongly in the infra-red, the heat contained in this part of the spectrum was absorbed in the thin water layer close to the wall, which in turn generated the boundary motion. As their chamber was illuminated from the side, their results are not readily applicable to the problem being studied here. However they do show the importance of fully incorporating the non-uniform absorption of the incoming radiation.

This paper reports an extension of TB's work, in which a more realistic model of the radiation source is used, and in which the long-timescale variation of the flow is investigated by experimental and numerical means. The radiation intensity is allowed to vary with depth, but with no horizontal dependence of the radiation field other than allowing for the opaque layer. It is assumed that the opaque surface layer prevents all radiation from entering the water below, and that there is no conduction into or other heating of the water. Thus the source term in the shaded region remains zero. It is further assumed that there are no obstructions to the flow, although in real lakes, the plant roots lying below the water add a further complication. However, experiments (Coates & Ferris 1992) on the effect of the plant roots on the flow showed that the root mat merely deflected the flow to pass underneath that mat, and that the scaling analysis described in §2 was still valid. The remainder of the paper is divided into sections which describe the experiment (§3) and the results (§4). Some numerical experiments are described in §5, and the conclusions are made in §6.

2. Formulation and scaling analysis

Under consideration is a rectangular cavity of height h and total length $(l+l_E)$, where l is the length of the opaque region, and l_E is the length of the transparent region, through which radiative energy enters (figure 2). The boundaries are rigid, and non-slip. The upper and lower boundaries are thermally insulated, while the endwalls are constant-temperature boundaries, held at the initial temperature T_0. The cavity

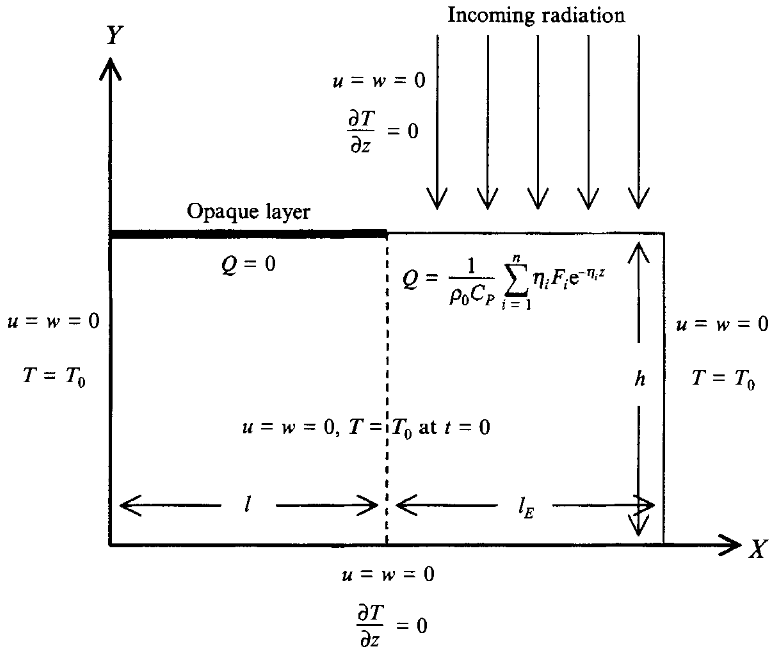

FIGURE 2. Sketch of the cavity with its boundary conditions.

contains a Newtonian fluid which is initially at rest and at temperature T_0. The usual Boussinesq equations describe the subsequent temperature and velocity fields:

$$\frac{\partial u}{\partial x} + \frac{\partial w}{\partial z} = 0, \tag{1}$$

$$\frac{\partial u}{\partial t} + u\frac{\partial u}{\partial x} + w\frac{\partial u}{\partial z} = -\frac{1}{\rho_0}\frac{\partial p}{\partial x} + \nu\left(\frac{\partial^2 u}{\partial x^2} + \frac{\partial^2 u}{\partial z^2}\right), \tag{2}$$

$$\frac{\partial w}{\partial t} + u\frac{\partial w}{\partial x} + w\frac{\partial w}{\partial z} = -\frac{1}{\rho_0}\frac{\partial p}{\partial z} + \nu\left(\frac{\partial^2 w}{\partial x^2} + \frac{\partial^2 w}{\partial z^2}\right) + g\alpha(T - T_0), \tag{3}$$

and

$$\frac{\partial T}{\partial t} + u\frac{\partial T}{\partial x} + w\frac{\partial T}{\partial z} = \kappa\left(\frac{\partial^2 T}{\partial x^2} + \frac{\partial^2 T}{\partial z^2}\right) + Q(x, z, t), \tag{4}$$

where u and w are the horizontal and vertical velocity components, T is the temperature, p is the pressure (incorporating the hydrostatic pressure), g is the acceleration due to gravity, and ν, ρ_0, α, and κ are the kinematic viscosity, density, coefficient of thermal expansion, and thermal diffusivity of the fluid at the temperature T_0. The source term $Q(x, z, t)$ is due to the absorption of the incoming radiation by the fluid. Given that the energy flux [W m^{-2}] as a function of depth is $F(z)$, the source term is given by

$$Q = \frac{1}{\rho_0 C_P}\frac{\partial F}{\partial z}, \tag{5}$$

where C_P is the specific heat at constant pressure for the fluid. The total flux is given by Beer's or Bouger's Law (e.g. Siegel & Howell 1981)

$$F(z) = \sum_{i=1}^{N} F_i e^{-\eta_i z}, \tag{6}$$

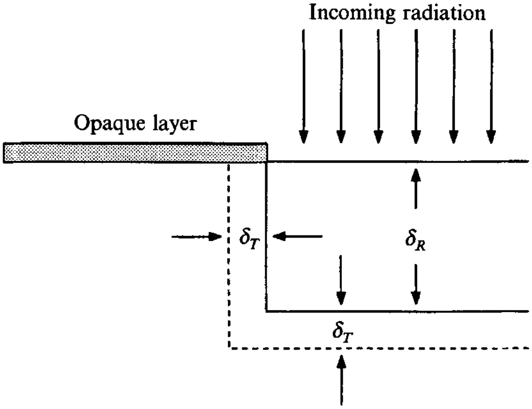

FIGURE 3. A sketch of the thermal and radiation lengthscales.

where the incoming radiation is divided into N wavebands. For each of these bands, the energy flux entering through the surface is F_i, and the attenuation coefficient η_i describes how the incoming radiation in the band is absorbed within the fluid column. Using (6) in (5), we can write the internal source term for this problem as

$$Q = \begin{cases} 0 & \text{for} \quad 0 \leqslant x < l; \\ \dfrac{1}{\rho_0 C_P} \displaystyle\sum_{i=1}^{N} \eta_i F_i \mathrm{e}^{-\eta_i z} & \text{for} \quad l \leqslant x \leqslant (l + l_E). \end{cases} \tag{7}$$

The determination of the parameters η_i and F_i will be discussed in §3.3.

2.1. *Scaling*

The general scaling for this problem is very complex, involving five distinct timescales. However, virtually all naturally occurring problems of this type fall into just one regime, and it is this regime that is to be discussed below. The reader is referred to Coates (1991) for the more detailed scaling.

When the radiation is initiated, it is absorbed in a layer of water beneath the transparent lid to some depth δ_R, while the water layer beneath the opaque lid remains unheated. Initially there is no fluid motion, so that the absorbed heat diffuses across and down, with the lengthscale $\delta_T \sim (\kappa t)^{\frac{1}{2}}$, as sketched in figure 3.

In the scaling that follows, a single or bulk value is required to parameterize both the incoming radiative energy over all the wavebands and the attenuation coefficients within those bands. These parameters are F_0 and η_b respectively, and were found by fitting the single-band model $F(z) = F_0 \exp[-\eta_b z]$ by a least-squares fit to the data points calculated with Beer's Law using the parameters F_i and η_i for the wavebands. The data points were located at depths z such that the energy absorbed between any two neighbouring points z_j and z_{j+1} was approximately constant.

At early times, the vertical diffusion lengthscale is unimportant, and the appropriate vertical lengthscale is $\delta_R \sim 1/\eta_b$. However, after some time t_{RC}, we will have $\delta_R < \delta_T$, and the vertical lengthscale will switch to δ_T. The transition time is, from $\delta_R \sim \delta_T$,

$$t_{RC} \sim h^2/\eta_*^2 \kappa, \tag{8}$$

where the dimensionless attenuation coefficient is defined as $\eta_* = \eta_b h$. We initially consider the scales for which $t < t_{RC}$. However, at early times, the only available horizontal lengthscale is δ_T.

The thermal balance is between the temperature increase and the source, and the flow is governed by a balance between acceleration and the buoyancy-induced pressure gradient. Thus from (3) we have

$$\frac{1}{\rho_0}\frac{\Delta p}{\delta_R} \sim g\alpha\Delta T, \tag{9}$$

and from (4)

$$\Delta T = \eta_b F_0 t/\rho_0 C_P, \tag{10}$$

where F_0 is the total radiation intensity at the surface. The energy input can be parameterized by the Grashof number,

$$Gr = g\alpha F_0 h^4/\rho_0 C_P \nu^3, \tag{11}$$

which is consistent with the usual definition of Gr if the radiation lengthscale in (10) is h (the radiation is absorbed over the entire cavity depth) and the timescale in (10) is h^2/ν. Thus (9) can be written as

$$\Delta p/\rho_0 \sim Gr\,\nu^3 t/h^4, \tag{12}$$

and, from (2),

$$u \sim \frac{Gr\,\nu^3}{h^4}\left(\frac{t^3}{\kappa}\right)^{\frac{1}{2}}. \tag{13}$$

The term $Gr\,\nu^3/h^4$ is just the buoyancy flux, but to maintain uniformity with other researchers in this area, the Grashof-number formulation will be used in the following.

This scale will hold until time t_c when the fluid will have travelled beyond the thermal diffusion lengthscale, and the appropriate horizontal lengthscale switches from δ_T to $\delta_c \sim ut_c$. From $ut_c \sim (\kappa t_c)^{\frac{1}{2}}$, and using (13), the transition time is

$$t_c \sim (\kappa h^4/Gr\,\nu^3)^{\frac{1}{2}}, \tag{14}$$

after which the inertia term dominates the unsteady term.

However, the development of the flow depends on two further timescales. These are the time t_ν at which the intrusion flow (13) becomes viscous, and the time t_E at which there is a balance between the energy being transported out by the intrusion and the energy being supplied by the radiation. The former occurs when $\delta_R \sim (\nu t_\nu)^{\frac{1}{2}}$, or at the viscous timescale

$$t_\nu \sim h^2/\eta_*^2 \nu, \tag{15}$$

and the latter when the energy per unit width entering the enclosure per unit time balances the energy per unit width per unit time being transported out over the depth δ_R with the current velocity scale u. This gives

$$F_0 l_E \sim \delta_R u \rho C_P \Delta T, \tag{16}$$

which simply reduces to $t_E \sim l_E/u$ using (10) for ΔT. We have defined l_E as the (exposed) length that is being illuminated by the radiation. Implicit in the existence of the energy-limited regime is the assumption that the intrusion has not yet reached the endwall of the bounded cavity. Defining the time to reach the endwall as $t_T \sim l/u$, the existence of the energy-limited regime requires that $t_E < t_T$, or simply that $A < A_E$ where $A_E = h/l_E$. We will assume that this condition is met in the following discussion, although flow regimes without an energy-limited velocity can be obtained from the appropriate scales to be described.

The flow development depends on the orderings of the timescales t_ν, t_E and t_c. We have ignored the timescale $t_\kappa \sim l^2/\kappa$, the time for thermal diffusion to penetrate the entire shaded length of the cavity, since even over a forcing time of 12 hours, conduction would only be important in cavities with a shaded length smaller than $l \sim 80$ mm. Neither natural lakes or the experiment to be described satisfy this requirement.

The scaling regime to be described requires that $t_c < t_\nu$ and $t_c < t_E$, and the conditions that result from these inequalities will be discussed shortly. This regime was considered in part by TB.

The initial unsteady velocity scale (13) will become inertial at the time t_c, and from the inertia–pressure balance

$$\frac{u^2}{\delta_c} \sim \frac{1}{\rho_0}\frac{\Delta p}{\delta_c}, \tag{17}$$

with the pressure difference (12), the inertial velocity is

$$u \sim (Gr\,\nu^3 t/h^4)^{\frac{1}{2}}. \tag{18}$$

These results were also obtained by TB. The unsteady velocity scale (13) is equivalent to u_0, equation (12) of TB, while the inertial velocity (18) is u_1 (equation (15) of TB). The transition time t_c is t_0 (equation (13) of TB). This scale depends only on the energy input to the fluid, and not on the depth of the absorption δ_R of the radiation. This result is perhaps surprising as one would intuitively expect that the energy being absorbed in a thin layer would accelerate the fluid more quickly than when the same energy is absorbed in a much thicker layer. While the temperature in the thinner layer certainly does increase more rapidly, with a corresponding increase in the vertical pressure *gradient* from (9), that gradient is determined over the vertical lengthscale, the inverse of which determines the temperature increase. The consequence is that the pressure itself remains independent of the vertical lengthscale δ_R, and the inertial velocity (18) in turn is independent of δ_R.

The subsequent flow development depends on when it becomes viscous or energy limited. The onset of viscous dominance is given earlier by (15), but now the onset of the energy-limited flow is given by (16), using the velocity (18), leading to

$$t_E \sim (h^4 l_E^2/Gr\,\nu^3)^{\frac{1}{3}}. \tag{19}$$

The viscosity/energy balance condition depends on the ratio t_ν/t_E, and using (15) and (19), we obtain the condition

$$Gr < \eta_*^6/A_E^2, \tag{20}$$

for viscosity to dominate first. If this condition is met, the timescale ordering is $t_c < t_\nu < t_E$, and the friction–pressure balance

$$\nu\frac{u}{\delta_R^2} \sim \frac{1}{\rho_0}\frac{\Delta p}{\delta_c}, \tag{21}$$

with the pressure difference (12), leads to the viscous velocity scale

$$u_\nu \sim (Gr\,\nu^2/\eta_*^2 h^2)^{\frac{1}{2}}. \tag{22}$$

This result is u_2, equation (20) of TB, where we have used $H_R \sim h/\eta_*$ as the equivalent penetration depth for this problem. The other scales of TB do not appear here, since we are considering just a single attenuation depth for the fluid. Further, TB examined an infinite cavity in which there is no energy-limited flow, so that there are no comparisons with the energy-limited scales obtained in this work.

(*a*)	$t_c < t_\nu < t_E < t_{RC}$ (13) → (18) at t_c (14) → (22) at t_ν (15) → (28) at t_E (27)	$Gr < \eta_*^6 A_E^{-2}$
(*b*)	$t_c < t_E < t_\nu < t_{RC}$ (13) → (18) at t_c (14) → (25) at t_E (19) → (26) at t_ν (15)	$\eta_*^6 A_E^{-2} < Gr$

TABLE 1. A summary of the convective regime showing the Grashof-number criteria, and the velocity scale development. The velocity scales are identified by their equation numbers in the text, as are the timescales at which the velocities change. The velocity-scale transitions are indicated by the arrow.

If the condition (20) is not met, the flow will become energy limited and the temperature ΔT will remain constant at the value it had at the time t_E

$$g\alpha \Delta T \sim \left(\frac{Gr\,\nu^3}{h^4}\right)\left(\frac{\eta *}{h}\right) t_E \tag{23}$$

obtained from (10) and (11). The pressure difference simply becomes

$$\Delta p/\rho_0 \sim (Gr\,\nu^3/h^4)\, t_E, \tag{24}$$

and substituting (24) with (19) into the inertia–pressure balance (17), the energy-limited velocity scale becomes

$$u_E \sim (Gr\,\nu^3 l_E/h^4)^{\frac{1}{3}}. \tag{25}$$

The energy-limited velocity scale (25) will also become viscous at t_ν, and in this case, the friction–pressure balance (21) with the energy-limited pressure, obtained from (24) with (19), gives the final velocity scale

$$u_{E\nu} \sim (Gr^2\, l_E^2/\eta_*^6\, \nu^3 h^2 t^3)^{\frac{1}{6}}. \tag{26}$$

This scale is inappropriate for the case $t_\nu < t_E$ when the velocity scale (25) becomes viscous, since the onset of the energy balance changes from that given by (19). Instead, the correct velocity scale to use in the derivation of t_E is (22) rather than (18), giving

$$t_E \sim (\eta_*^2\, h^2 l_E^2/Gr\,\nu^2)^{\frac{1}{2}}, \tag{27}$$

which when substituted into (24) gives

$$u_{\nu E} \sim (Gr\,\nu^2 l_E^2/\eta_*^2\, h^2 t^2)^{\frac{1}{4}} \tag{28}$$

using the friction–pressure balance (21).

The two velocity scales (22) and (25) show that once $t > t_\nu$ or $t > t_E$, the velocity no longer depends on time, indicating that the flow reaches a steady state until both t_ν and t_E are exceeded. In this case, the velocity scale becomes either (26) or (28). The time dependence of these scales results from the fact that as energy is being advected away by an intrusion whose depth increases as a function of $t^{\frac{1}{2}}$ due to the effects of viscosity, the velocity must decrease as a function of $t^{-\frac{1}{2}}$ to maintain the balance between energy input and output. However, the inertial scale (18) and the energy-limited scale (25) do not show any depth dependence because the pressure gradient itself is independent of δ_R as discussed above. In these regimes, the intrusion depth scale is δ_R.

This regime is summarized in table 1. For times greater than t_{RC}, the vertical lengthscale becomes δ_T, and a new set of scaling relationships will apply. Although these scales are available, t_{RC} is typically much larger than any of the scales relevant to limnological situations, and the details are omitted here.

3. Experimental procedures

3.1. *Description*

A series of experiments was performed to test aspects of this scaling. The experimental tank was a Perspex box immersed in a constant-temperature bath filled with filtered water. The tank was constructed from 10 mm Perspex, except for the 20 mm thick main sidewalls, and consisted of three separate chambers (figure 4). The largest of these was the experimental cavity with an internal size of total length $(l+l_E) = 600$ mm, height $h = 300$ mm, and width 200 mm. To one side of this was a smaller chamber of the same width and height as the main cavity, but only 90 mm in length, used to obtain the radiation profiles, as described below. Beneath both of these was the third tank, running the entire length, but of an internal height of only 100 mm. Its purpose was to prevent bottom heating of the main cavity by radiation which penetrated the full depth to be absorbed at the base. Instead, the radiation continued through the lower tank, and was absorbed by a matt black coating on its base. Any thermal re-emission by the base was by long-wave radiation, and this was completely absorbed by the water circulating through the lower tank from the constant-temperature bath so that it did not reach the base of the experimental cavity. The tank was filled with the filtered water from the constant-temperature bath to ensure that both the tank and the bath were isothermal.

The top of the tank had two separate Perspex lids. The lower of these sat directly on the water surface, and formed the upper non-slip boundary. The upper lid, in the form of a tray, rested on spacers on the first lid to leave a 4 cm air gap between the two. The air gap formed the upper insulating boundary. The tray also held the blocking layer, a section of aluminium foil covering one half of the surface, which prevented the radiation from entering that half of the tank. When required, it also held the infra-red filter. The latter took the form of a 10 mm thick water layer, the depth being set by a 10 mm lip on one side of the tray. Water absorbs strongly in the infra-red, and this thin layer removed the bulk of the infra-red component from entering the experimental cavity.

The light source used in the experiments was the Prolite company's Profile Follow Spot theatre lamp, containing a 1000 W quartz globe, chosen as it provided an intense light source that had maximum parallicity and uniformity. The former ensured that there was a sharp vertical boundary between the light and dark regions, and the latter ensured that the flow remained two-dimensional, with no local bright spots to cause uneven heating of the water in the cavity. The separation between the light and the tank was 1580 mm, chosen to ensure that half the tank was illuminated at the maximum possible light intensity, without using the outer regions of the light beam. The separation was achieved by using the lamp in a horizontal position, and bending the beam into the vertical with a plane mirror.

The temperatures were measured by placing thermistors through small holes drilled in the trays at fixed locations down the centreline of the tank. The locations were in the shaded region at distances of 215, 150, 85, and 20 mm from the light/dark boundary. These locations were chosen to enable the intrusion to be tracked as it passed each thermistor in turn. Earlier trials had indicated that the maximum intrusion velocities were at a depth of approximately 20 mm, and the thermistors were located at this depth, with an accuracy of ± 1 mm.

Thermometrics FP07 thermistors were used, and each was located at the tip of a 2 mm diameter stainless steel tube, covered in an insulating white heat-shrink plastic to prevent conduction of heat down the tubes. White plastic was used to minimize the heating of the tubes by absorption of the incoming radiation. The thermistors were

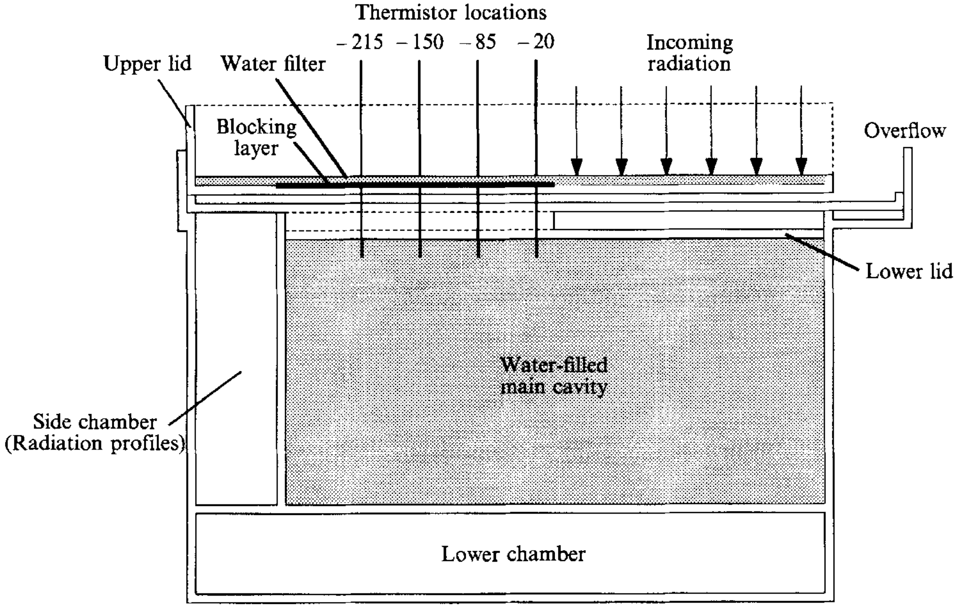

FIGURE 4. A schematic of the experimental set-up, which shows the two lids in place, and with the experimental cavity filled (the shaded region in the sketch). The blocking layer ensures that the left side is not illuminated. The thermistor positions are also shown.

placed in the tank shortly before the experiment was started to minimize any heat conduction between the cavity and the exterior. Their depth was set by placing a tightly fitting rubber O-ring at the required position on each thermistor tube; the O-ring rested on the surface of the upper tray. The thermistor voltages were sampled at 5 s intervals and were converted to temperatures by a third-order polynomial determined by calibration against a precision mercury thermometer. The absolute temperature data were accurate to 0.01 °C.

3.2. *Velocity measurement*

The velocities were measured by a pattern tracking technique first used to measure cloud motion (Leese, Novak & Clarke 1971) and automated by various researchers (Ninnis, Collins & Emery 1986; Collins & Emery 1988) to measure Arctic ice motion. It was adapted by Stevens & Coates (1993) for small-scale laboratory experiments, and as it is fully described there, only a brief description will be given here. After the tank had been filled with filtered water, particles of Pliolite, ground to a size smaller than 75 μm, were added as the tracer. During the experiments, the centreline of the tank was illuminated by a 10 mm laser light sheet, and the particle images were recorded by a video camera with a laser line filter attached. The latter ensured that the light source driving the flow was not recorded onto the video tape. For each time t at which the velocity field was to be determined, a pair of images, separated by some time interval Δt, was obtained from the video recording. From the first image of this pair, a number of smaller sub-images were extracted, each centred on a location (x_i, z_i) at which the velocity was required. These sub-images, each of some size $l_w \times l_w$ pixels, were called the source windows. Next, a number of larger sub-images of size $l_s \times l_s$ pixels were extracted from the second image of the pair, each centred at the same locations (x_i, z_i). These were the search windows. Finally, the pattern matching was performed by finding the maximum cross-correlation between the search and source windows, giving rise to the name MCC for the technique. In essence, each source window was moved to all possible positions in its corresponding search window, the correlation at each position calculated, and the location (x_m, z_m) of the maximum correlation recorded as this corresponded to the best pattern match between the search and source windows. From the shift $(x_m - x_i, z_m - z_i)$ between the location of the source window and the location of the maximum correlation over the time interval Δt between the image pairs, the velocity at (x_i, z_i) could be calculated.

Trials were run to determine the optimum sizes $l_w < l_s$ of the source and search windows, and the interval Δt between the image pairs. Reducing the sizes reduced the computational overhead, but also reduced the reliability by having fewer patterns that could be matched. However, increasing the sizes above some optimum value meant that any variability within the sub-images would also reduce the reliability. Small velocities also reduced the computational overhead since the search window could be smaller, but at the cost of reduced resolution. From the trials, optimum values were determined, and these were used in all subsequent correlations.

The size of the images for these experiments was determined by the desire to achieve a velocity resolution of at least 5%. Since the MCC technique described has a resolution of ± 1 pixel, a 5% velocity resolution required that the fluid travel at least 20 pixels during the time interval Δt between the each image of the MCC pair. The interval Δt was typically 4 s. However, at the small velocities (of order of 1 mm s^{-1}) indicated by the earlier trials, the real horizontal distance covered during the time Δt was approximately 5 mm. Setting this distance to correspond to a 20 pixel section of the image, the full image size of 768 pixels limited the coverage to approximately 200 mm of the tank.

Another limitation was the necessity to resolve each particle of the tracer. Since they are of small size, the image section could be no larger than approximately 200 mm to be able to resolve the particles. Given this image size, the video camera was positioned so that as much as possible of the shaded region was visible whilst still keeping the light/dark boundary in view. In the actual experiments performed with these settings, described in §4, it was found that one pixel spanned a distance of approximately 0.1 mm. As the velocity resolution of the technique was of the order of one pixel per second, the experimental error in the velocity was estimated as 0.1 mm s^{-1}.

3.3. *Parameter determination*

A method that enabled the spectral parameters to be determined for each experimental run was developed. If the radiation uniformly illuminated the water surface, the water stratified, there was no fluid motion and the energy redistribution within the water was by conduction alone. The temperature as a function of the depth z and time t for a conducting solid with insulating boundaries and an internal source term of the form of (7) is (Carslaw & Jaeger 1978)

$$T(z,t) = \sum_{i=1}^{N} \left\{ \frac{F_i}{\rho_0 C_P h}\left(1-\mathrm{e}^{-\eta_i h}\right) t + \frac{2\eta_i^2 F_i h^3}{\kappa \pi^2 \rho_0 C_P} \sum_{n=1}^{\infty} \left(\frac{1-(-1)^n \mathrm{e}^{-\eta_i h}}{\eta_i^2 h^2 + n^2 \pi^2} \right) \left(\frac{1-\mathrm{e}^{-\kappa n^2 \pi^2 t/h^2}}{n^2} \right) \cos \frac{n\pi z}{h} \right\}, \tag{29}$$

where the parameters are defined earlier (§2). Thus for a given temperature profile at a particular time, the values for F_i and η_i could be adjusted until (29) matched the given profile. To do this, the small side chamber was illuminated, and the temperatures were measured at nine depths. The thermistors were located at fixed depths for each experiment but these were altered as required to obtain a good temperature profile with depth as the parameter determination runs were repeated. The temperatures were measured after one hour to ensure that the deeper water was heated sufficiently for an accurate temperature measurement to be made.

A constraint imposed on the fluxes in each band is that they must be realistic. Using the water attenuation coefficient data of Hale & Querry (1973), the waveband limits could be determined for each of the values η_i found using (29). Using these limits, the flux F_i within each band of a black body at the same temperature as the lamp could be estimated. These values were then used in (29) from which a better estimate for the η_i could be made. This procedure was repeated iteratively until the error between the theoretical and measured profiles was a minimum.

Further experiments were performed with the pliolite resin added at the required concentration. There was no measurable change in the temperature profiles, and so for these experiments, the use of Beer's law remains justified with and without the scattering particles.

4. Results

4.1. *Experimental parameters*

Three sets of experiments were run. The first set used the lamp at its maximum intensity, while the second set reduced the intensity of the lamp (and therefore the Grashof number) with a neutral density filter. The spectral composition of the lamp was unaltered by this filter. The third set of experiments used an infra-red filter which altered the spectral characteristics as well as reducing the surface flux of the radiation entering the experimental chamber. As discussed above, the infra-red filter consisted of a 10 mm deep water layer held in the upper tray.

Prior to the experiments, the radiation parameters were calculated using the technique described in §3.3. The thermistors were set at the required depth in the side chamber, and the temperature/depth data were measured after one hour for the three experimental cases being considered (figure 5). An additional constraint imposed was that any manipulation of the parameters for one experiment must be reflected in the remainder. Thus, while the neutral density filter reduced the intensity F_i by the same fraction in all wavelength bands, the water filter in the upper tray altered the intensity in each band by a different amount. The latter could be determined by calculating from Beer's law (6) how much of the incoming intensity penetrated the 10 mm deep water layer in the upper tray. A least-squares analysis of the data showed that a three-band model could accurately reproduce the observed data; the resulting radiation parameters are given in table 2, along with the appropriate waveband limits from the data of Hale & Querry (1973).

As a check on the method, the energy distribution within the three wave bands of a 3200 K black body, approximately equivalent to the lamp, was determined. The energy fluxes of table 2 were consistent with this distribution. Using the data of table 2, the bulk surface flux and the bulk attenuation coefficient were found for each of the experiments, from which the corresponding Grashof number, from (11), and dimensionless attenuation coefficient, defined by $\eta_* = \eta_b h$, could be determined. The bulk values thus found are given in table 3. The Prandtl number of the experiments was $Pr = 7.04$.

These values for Gr and η_* immediately place the experiments into the regime described in §2, since using (20), the condition

$$\eta_*^6/A_E^2 < Gr \tag{30}$$

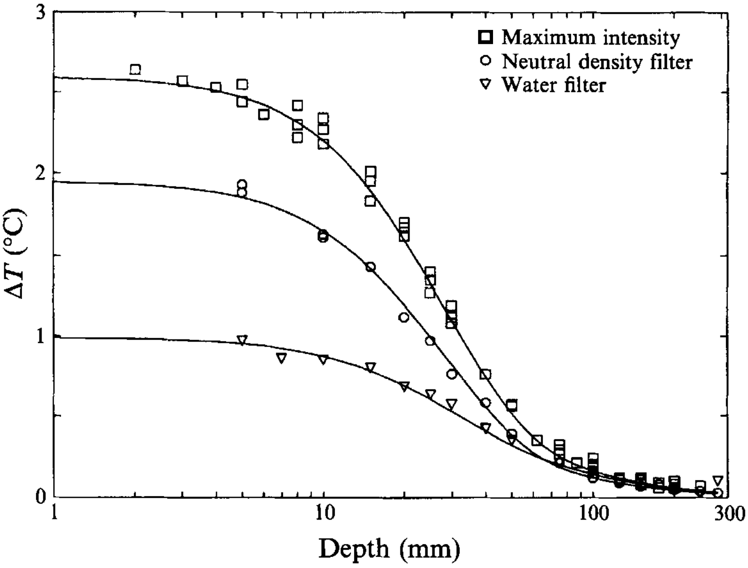

FIGURE 5. A plot of the measured temperature/depth data for the three experiments, acquired after the water had been heated for one hour. The analytical profile of the best-fit three-band model for each of the three experiments is also shown.

Band	Wavelength (nm)	Percentage total energy	F_i (W m^{-2}) MAX	WF	ND	η_i (m^{-1})
1	> 1200	~ 50%	64.5	18	48.5	145
2	800–1200	~ 30%	39	33.5	29	15
3	< 800	~ 20%	24	23.5	18	2.5

TABLE 2. The best-fit three-band model for the surface energy flux F_i and attenuation coefficient η_i to the temperature/depth data. The surface fluxes for the three experiments are given in the columns MAX (maximum intensity), WF (water filter) and ND (neutral density filter).

Experiment	F_0 (W m^{-2})	Gr	η_b (m^{-1})	η_*
Maximum intensity	115	4.33×10^8	21.6	6.48
'Water' filter	64	2.41×10^8	15.6	4.68
Neutral density filter	87	3.28×10^8	21.6	6.48

TABLE 3. The bulk values for the surface flux F_0 and the attenuation coefficient η_b for the three experiments. The equivalent Grashof number and dimensionless attenuation coefficient are also given.

Experiment	t_c (s)	t_E (s)	u_E (mm s^{-1})	t_v (s)
Maximum intensity	1.7	119	2.5	2140
'Water' filter	2.2	145	2.1	4110
Neutral density filter	1.9	131	2.3	2140

TABLE 4. The time and velocity scales expected from the scaling, where t_c is given by (14), t_E by (19), u_E by (25), and t_v by (15).

is satisfied for all three experiments. Using (14), (19), (25) and (15) and the parameters of table 3, the expected time and velocity scales can be calculated for the three experiments. These are given in table 4.

4.2. *Experimental results*

4.2.1. *Velocity vectors*

Using the MCC technique, the velocities were measured for the three experiments, and the early stages of the flow are shown in figure 6(*a–d*) for the maximum intensity experiment, figure 6(*e–h*) for the water filter experiment, and figure 6(*i–l*) for the neutral density filter experiment. The times at which the velocities were measured are shown on each of the figures, as are the dimensions of the image section used for each of the experiments. As discussed in §3.2, the latter results from the requirement to adequately image the tracer particles and to ensure a reasonable velocity resolution, which limited the size of the image that could be used in the velocity measurement.

Considering the maximum intensity experiment of figure 6, the vector plots show the development of the intrusion. It was only just detectable at 50 s (figure 6*a*), but had become quite distinct after 100 s (figure 6*b*). The approximate boundary of the intrusion, at which the velocity had reduced to 20% of the maximum value, has been sketched on figure 6(*a–d*) to help delineate the intrusion since, as it advanced along the shaded region, it displaced fluid away and downwards, resulting in velocity vectors which appear to increase the size of the intrusion. The intrusion was well established after 150 s (figure 6*c*), and by 200 s (figure 6*d*), it was approaching the limits of the images used in the velocity measurement. Velocities continued to be measured at later times, but these are not shown.

Similar results were obtained for the other two experiments. The smaller energy flux entering the water filter experiment resulted in a slower acceleration of the flow. In this case, the intrusion could only be detected by 150 s (figure 6*e*), although by 200 s (figure 6*f*), it had become distinct. It was fully developed by 250 s (figure 6*g*), and had reached the image limits by 300 s (figure 6*h*). The energy flux for the neutral density filter experiment was midway between the previous values, and the timings are also intermediate. Here the intrusion had become detectable by 100 s (figure 6*i*), but was well developed by 150 s (figure 6*j*). It reached the image limits by 250 s (figure 6*l*). However, the intrusion boundary is less distinct in this experiment, with the greater spread in the velocity magnitudes giving a larger velocity field outside the apparent intrusion boundary. The broader intrusion may have been due to a change in the lamp intensity and spectrum prior to a lamp failure.

At all times in these experiments, the intrusion appears as a single entity; that is, there is no evidence of a number of smaller intrusions corresponding to the different F_i and η_i of the incoming radiation. In addition, the use of the single bulk value to predict the intrusion thickness gives a value that is of the same order as the measured value, as shown by a comparison of the measured and theoretical values of the intrusion thickness for each of the three experiments (table 5). This fact strengthens the argument that describing the flow by a single set of bulk parameters is justified.

4.2.2. *Temperature profiles*

Thermistor temperature data were available for repeated runs of both the maximum intensity and the water filter experiments. The temperature increases from the thermistor data for three repeated runs are plotted against time in figure 7, where the thermistors were set at a depth of 20 mm, and were located in the shaded region at distances of 20, 85, 150, and 215 mm from the light/dark boundary. Figure 7(*a*) shows

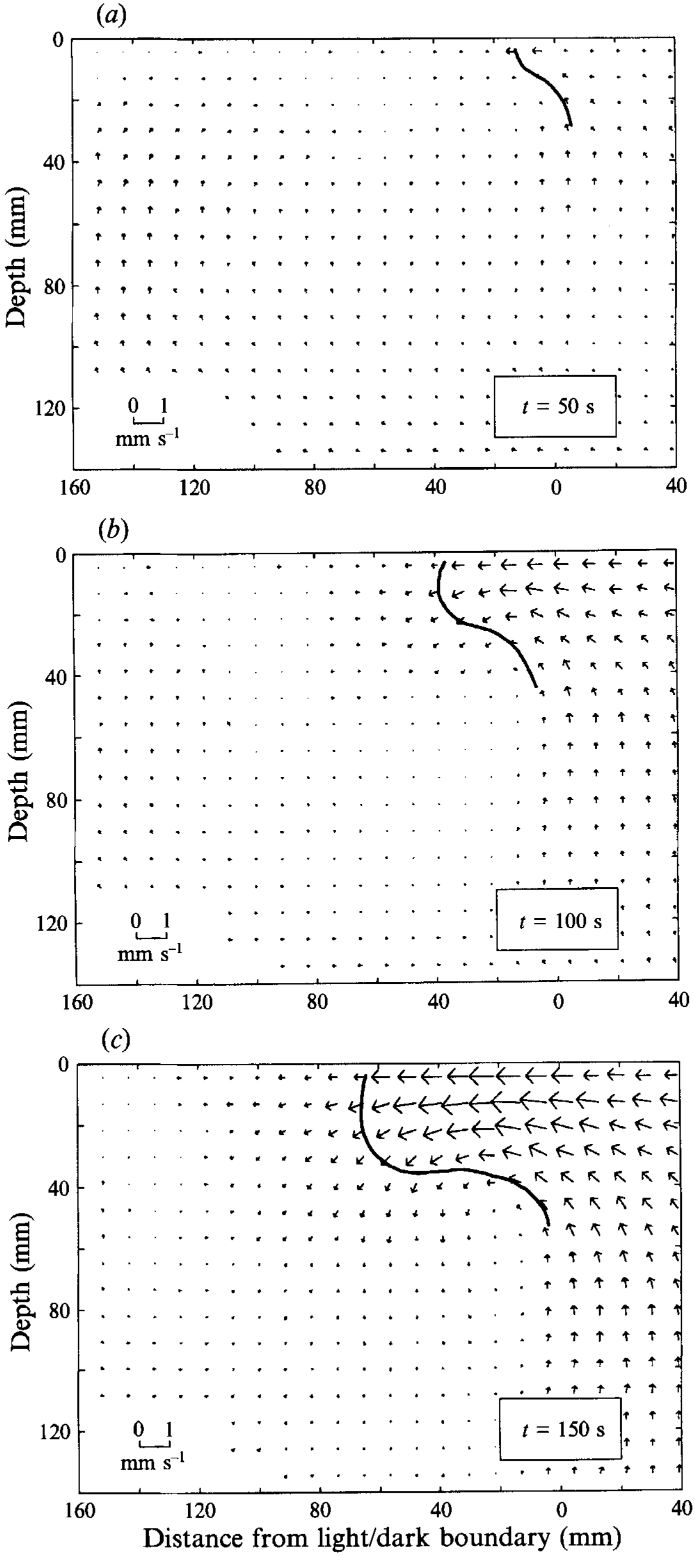

FIGURE 6(a–c). For caption see page 151.

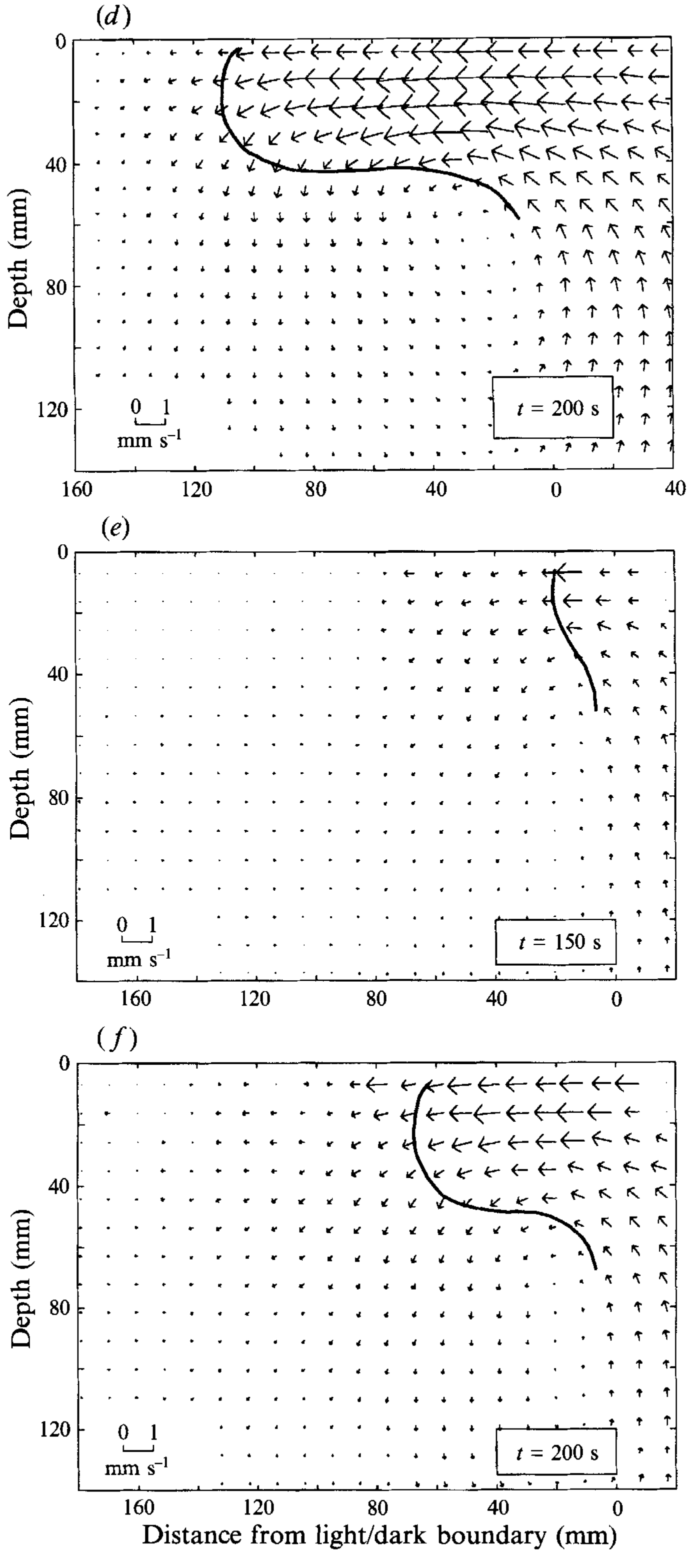

FIGURE 6(*d–f*). For caption see page 151.

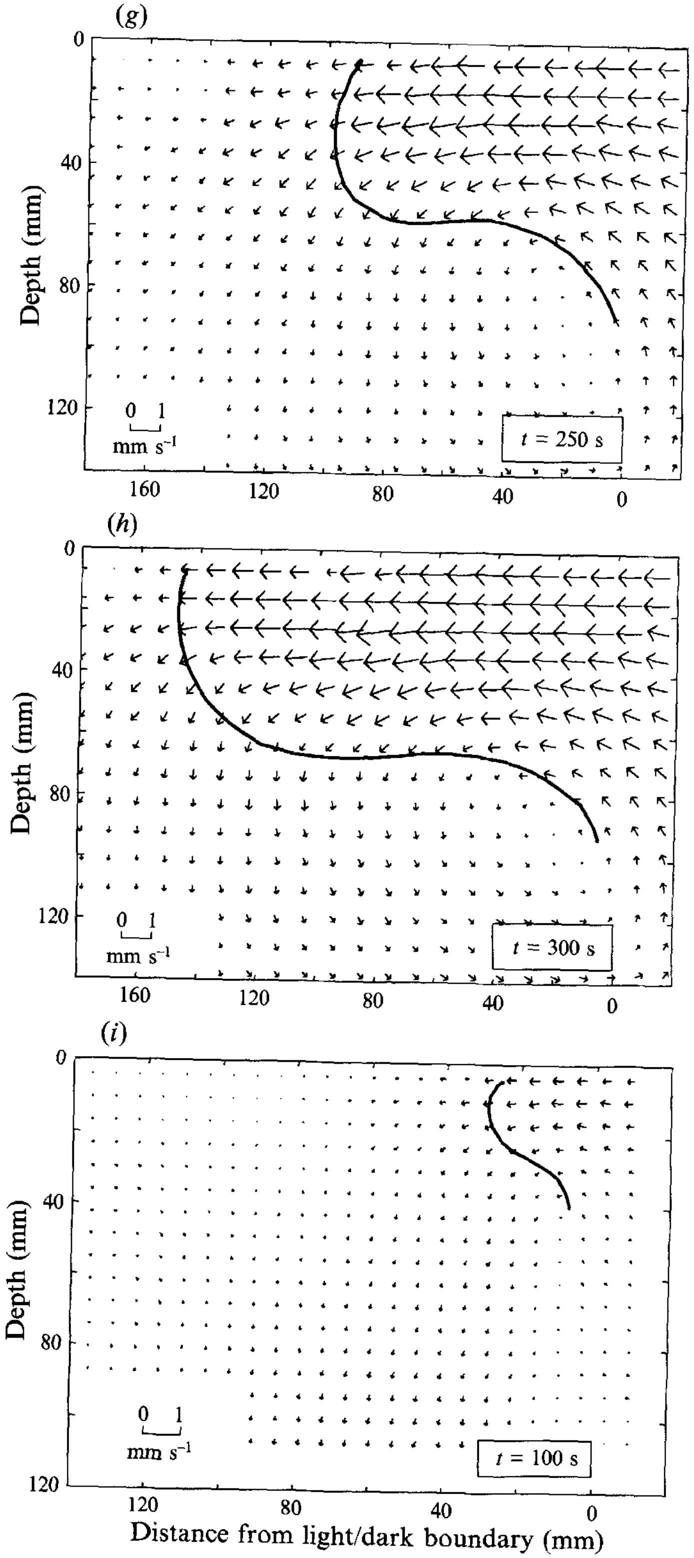

FIGURE 6(g–i). For caption see page 151.

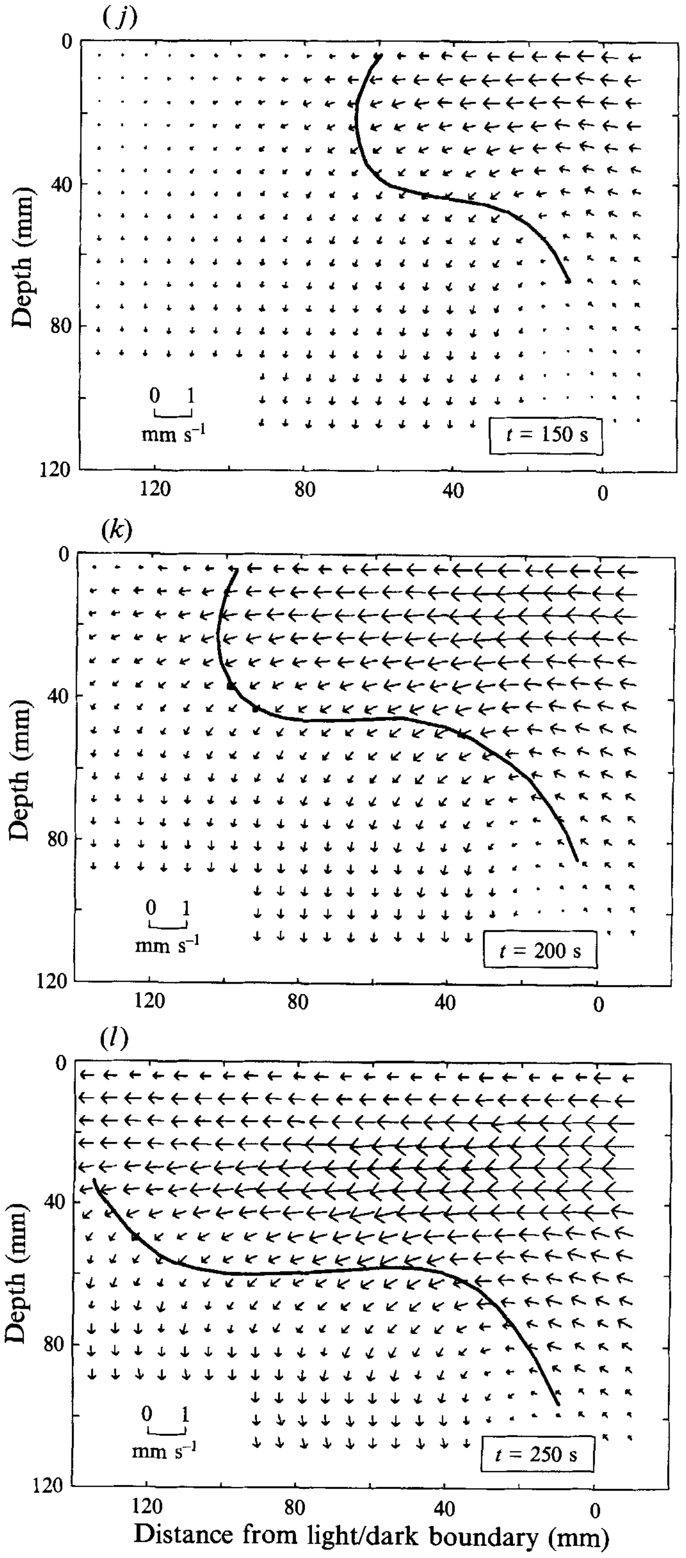

FIGURE 6(j–l). For caption see facing page.

Experiment	η_b (m^{-1})	Theoretical (mm)	Measured (mm)
Maximum intensity	21.6	46	30
'Water' filter	15.6	64	50
Neutral density filter	21.6	46	40

TABLE 5. The theoretical intrusion thickness obtained from the bulk attenuation coefficient ($1/\eta_b$) is compared with the thickness measured from the three experiments.

the results for the maximum intensity experiment, and figure 7(*b*) those for the water filter experiment.

Considering the maximum intensity experiment, the passage of the intrusion can be seen in the temperature data. Initially all thermistors recorded $\Delta T = 0$ °C, but at approximately 75 s, the temperature of the thermistor at 20 mm began to rise as the intrusion reached that location. The time is accurate to ± 10 s, obtained from the repeated runs of figure 7(*a*). By 190 s, the intrusion has reached the thermistor at 85 mm, as can be seen by the sharp lifting off of the temperature profile. The sharp rise was because the warmer water was travelling faster and caught up with the cooler and slower water forming a sharp front. After the passage of the front, the slope of the temperature/time trace reverted to a similar slope as for the thermistor at 20 mm, indicating that approximately equal quantities of heat were advected past both thermistors.

The intrusion reached the thermistor at 150 mm at 260 ± 10 s, followed by a similar steep rise during the passage of the front. The slope then became approximately linear but with a higher value than at the previous locations since at this later time, the intrusion was travelling faster and advected more heat from the illuminated area past the thermistor. By 320 s, the intrusion has reached the final thermistor at 215 mm, which again showed the sharp temperature rise during the passage of the front, before the slope decreased to a short linear region, steeper again as expected since the intrusion was even faster here.

A short time later, the intrusion struck the endwall of the tank, and as the effect of this travelled back along the tank, it distorted the temperature (and velocity) profiles of each thermistor in turn. This occurs at approximately 500 s for the thermistor at 215 mm, and at slightly later times for the remaining thermistors. These temperature results suggest that the velocity data are good to approximately 550 s for a location at the light/dark boundary before the distortion due to the reflection is felt.

While it was attempted to keep the initial conditions for each experiment the same, some variations still remained. One particular problem concerned the endwalls. Very slight temperature differences at the endwalls were sufficient to generate small plumes. These could be detected when the experiment was set up for velocity measurement by particle pattern tracking. Using the water bath, the endwall temperature was controlled to minimize the plumes. However, some experiments were run to measure just the temperatures, and for these, no such plumes could be detected. This may be another

FIGURE 6. The velocity vectors over a section of the tank obtained by the MCC technique are shown for the times (*a*) $t = 50$ s, (*b*) $t = 100$ s, (*c*) $t = 150$ s, and (*d*) $t = 200$ s for the maximum intensity experiment; (*e*) $t = 150$ s, (*f*) $t = 200$ s, (*g*) $t = 250$ s, and (*h*) $t = 300$ s for the water filter experiment; and (*i*) $t = 100$ s, (*j*) $t = 150$ s, (*k*) $t = 200$ s, and (*l*) $t = 250$ s for the neutral density filter experiment. The light/dark boundary is at $x = 0$, and the surface of the tank is at $z = 0$. The shaded region is to the left of the light/dark boundary. All distances are in mm. The velocity magnitude is indicated by the scale bar. The times at which the velocities were measured are shown on the figures.

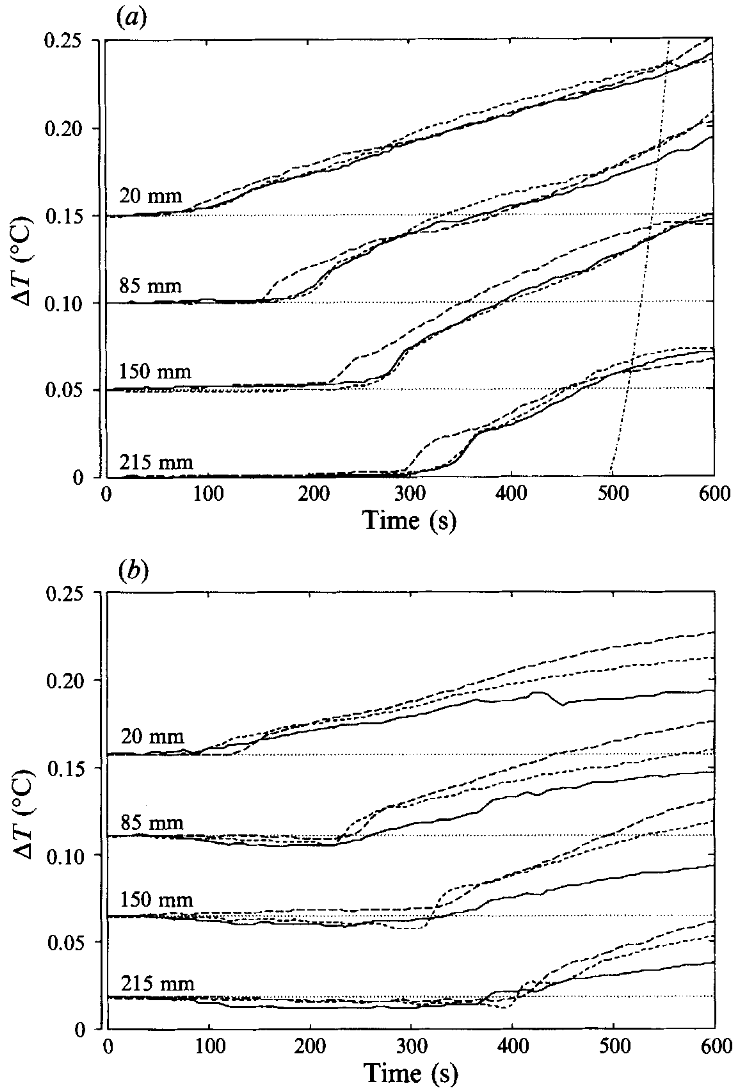

FIGURE 7. The temperature increases from the thermistor data for three repeated runs plotted against time. The thermistors were set at a depth of 20 mm and in the shaded region at the distances from the light/dark boundary shown on the plots. Results from (*a*) the maximum intensity experiment and (*b*) the water filter experiment are shown. The solid line corresponds to the experiment for which velocities were acquired. The dot-dash line in (*a*) is the time at which endwall effects influence the temperature data.

cause of the variation observed in the temperature data. However, except for the lift-off times, all the data show the same features, and so are included in figure 7(*a*). Another possible reason for the apparent temperature variation is the uncertainty in the thermistor depth. The temperatures have the greatest variation near the surface where the radiative heating is at its greatest value, so that a small error of ± 0.5 mm in position may cause an error of up to 5% in the measured temperatures.

Similar temperature results were obtained for the water filter experiment. The temperature increases from the thermistor data were plotted against time in figure 7(*b*) for repeated runs of this experiment. The slower acceleration of the intrusion in this experiment can be seen in the longer time of 105 s before the temperature at 20 mm began to rise as the intrusion reached that thermistor location. The time is accurate to ±15 s, obtained from the repeated runs of figure 7(*b*). By 220 s, the intrusion had reached the thermistor at 85 mm, with the temperature/time trace showing the same sharp lifting off due to the passage of the front as seen in the maximum intensity experiment. After the passage of the front, the temperature rise reverted to a similar slope as recorded by the thermistor at 20 mm. The intrusion front reached the thermistor at 150 mm at 315 s, but the passage of the front was not as distinct in the data at this location, with considerable variation in the temperature values. As discussed earlier, the temperature differences being measured are very small, and they are sensitive to slight errors in location. What can be seen is that the slope was greater than at the previous location since, as in the maximum intensity experiment, the intrusion was travelling faster by this time, and it advected more heat from the illuminated area past the thermistor. By 390 s, the intrusion had reached the final thermistor at 215 mm, with a short linear region in the temperature data of the same order as the previous location. The effect of the reflection against the endwall cannot be seen in the temperature profiles of figure 7(*b*), suggesting that the velocity data are good to at least $t = 600$ s. Variations in the thermistor positions and the initial conditions for the experiments, and difficulties in detecting possible endwall plumes in some experiments are the possible causes of the variations observed in the temperature data.

The initial small temperature decrease observed is probably due to a combination of two effects. A small stratification (~ 0.01 °C) in the tank was inevitable during the several hours that were required for the filling motions to damp out. When combined with a very small upwelling in the shaded region which existed prior to the experimental run, enough cooler water could be advected past the thermistors to register the slight temperature drop. The upwelling was most likely a boundary-generated plume, but being very small, it remained undetected.

4.2.3. *General results*

The maximum values of the velocity at the light/dark boundary are plotted as a function of $t^{\frac{1}{2}}$ for the three experiments in figure 8. The errors bars are set to the estimated velocity error of the MCC technique, namely 0.1 mm s^{-1}.

Advection should become important after the timescale t_c, given in table 4, but the experimental data indicate that the flow does not become inertial until a time an order of magnitude larger (20 s, 60 s, and 40 s for the maximum intensity, water filter, and neutral density filter experiment respectively). The reason for this discrepancy is unexplained.

In the inertial regime, the velocity is expected to be linear with respect to $t^{\frac{1}{2}}$ from (18), and the data of figure 8 show that the maximum velocities for each experiment do fall well on a straight line. This confirms that the early stage of the flow is indeed inertial. However, the scaling suggests that the inertial velocity scale (18) depends only on the incoming energy flux, and not on how that energy is distributed within the water column. To investigate this assertion, the maximum horizontal velocities for the three experiments (obtained from figure 8) are plotted against $(Gr\,\nu^3 t/h^4)^{\frac{1}{2}}$ in figure 9. We already know that each of the flows is initially inertial, but we can see from figure 9 that there is a reasonable fit to the same line for all three experimental results, confirming the prediction of (18).

We can obtain further confirmation by using the inertial velocity to predict when the intrusion should reach each thermistor in turn, and comparing this time with that

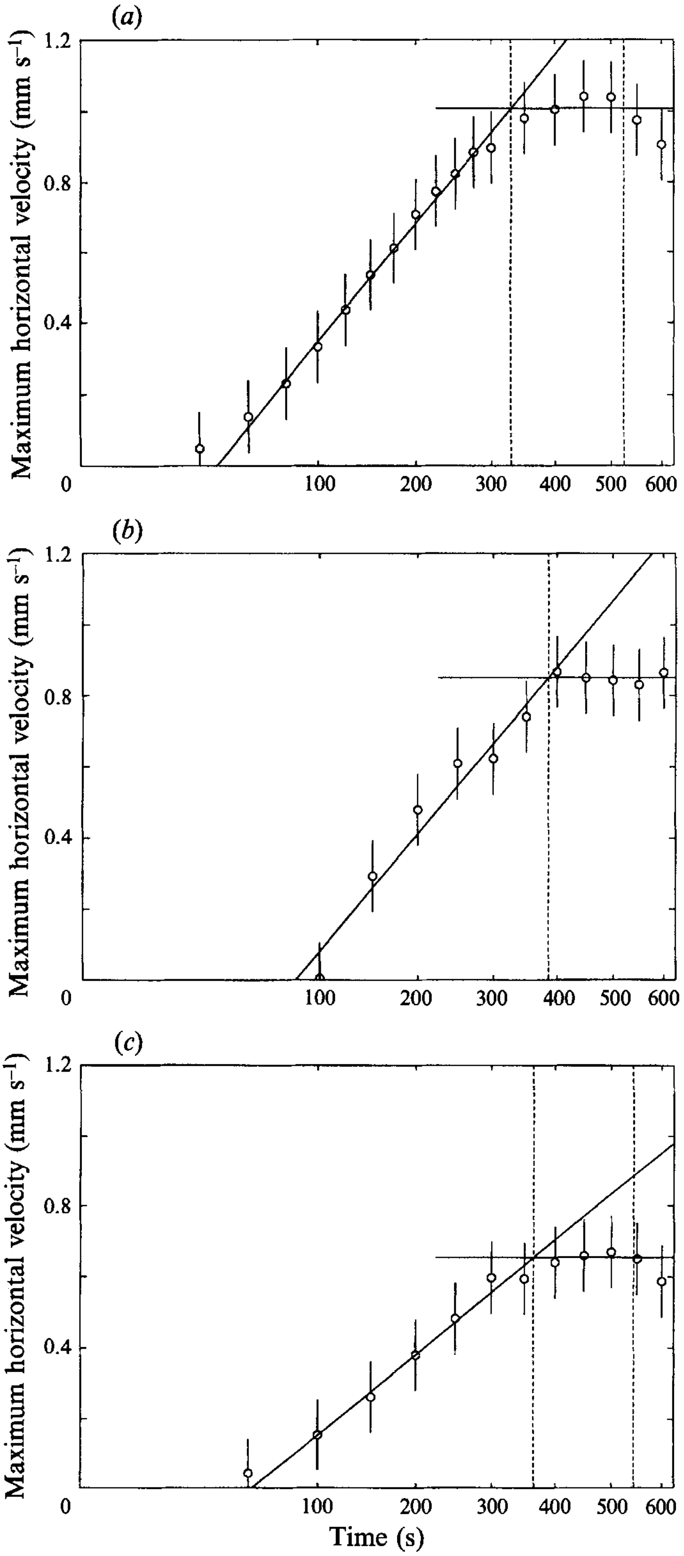

FIGURE 8(*a–c*). For caption see facing page.

obtained from the temperature data of figure 7. Performing an analysis similar to that used to obtain figure 9, a line of best fit to the maximum horizontal velocity gives

$$u = 0.484\left(\frac{Gr\,\nu^3 t}{h^4}\right)^{\frac{1}{2}} - 0.56\times 10^{-3}\ \mathrm{m\ s^{-1}}. \tag{31}$$

The distance s travelled by the intrusion as a function of time can be found by integrating (31), yielding

$$s = \left(\frac{h^4}{Gr\,\nu^3}\right)\left\{322\left(\frac{Gr\,\nu^3 t}{h^4}\right)^{\frac{3}{2}} - 0.556\left(\frac{Gr\,\nu^3 t}{h^4}\right) + 2.46\times 10^{-7}\right\}\ \mathrm{mm}, \tag{32}$$

where the constants have been adjusted to give the distance in millimetres. Table 6 gives the predicted and actual times that the intrusion reaches each of the thermistors for both the maximum intensity and water filter experiments. The agreement between these times is reasonable, and is further confirmation that the inertial regime depends only on Gr.

Figure 8 also shows that after a period of time the velocity in each of the three experiments becomes constant, which is consistent with the energy-limited regime. The time at which this occurs for the three experiments can be measured from figure 8, and is summarized in table 7 along with the value expected from the scaling relation (19). The measured and the scaling values are comparable, with the ratio t/t_E being independent of the experiment being run, suggesting that the ratio is independent of the attenuation coefficient, as expected from (19).

While the energy-limited velocities for each of the different experiments are constant, as expected from the scaling relation (25), their reduction to a single velocity value based on the effective flux is not, with some variation between experiments. This can be seen in figure 10, which shows the velocity, scaled with respect to u_E, plotted against time. The theoretical value u_E is obtained from table 4. The average experimental velocity for each experiment is given in table 8, along with the ratio u/u_E. The agreement for two of the experiments is very good. The velocities of the neutral density filter experiments are generally lower than predicted and, as noted earlier, the energy input and its distribution for this experiment may not have been as originally measured. It is possible that the lamp intensity was reduced prior to a lamp failure.

5. Numerical experiments

5.1. *Non-dimensionalization and numerical scheme*

While the experimental data confirmed the scaling relations to a degree, the Grashof numbers varied over only a limited range. To extend this range, a series of numerical experiments were also performed.

The numerical scheme used to solve equations (1)–(4) is based on the usual SIMPLE scheme but defined on a non-staggered grid. The problems of non-elipticity, resulting in oscillations of the pressure field, were overcome by the use of an elliptic pressure term derived by Armfield (1991), and is fully described there. The discretization is

---

FIGURE 8. The maximum value of the horizontal velocity data at a position just inside the shaded region is plotted against $t^{\frac{1}{2}}$ for (*a*) the maximum intensity experiment, (*b*) the water filter experiment, and (*c*) the neutral density filter experiment. The inertial regime is shown with the straight line of best fit to the data. Also shown (dashed line) is the time at which the velocity becomes constant, consistent with the energy-limited regime. The second dashed line in (*a*) and (*c*) is the time at which the interaction of the flow with the endwall begins to distort the flow.

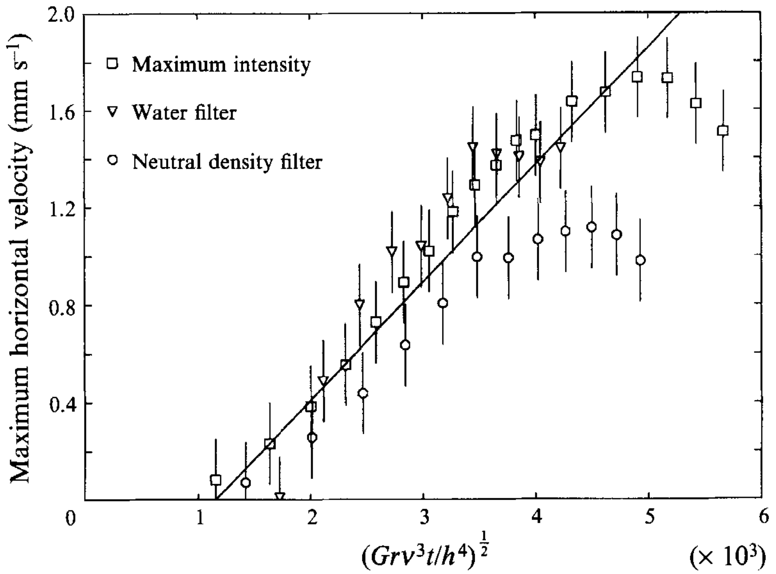

FIGURE 9. The maximum velocity data for all three experiments plotted against $(Gr\,\nu^3 t/h^4)^{\frac{1}{2}}$. The inertial regime is shown with the line of best fit to the data. This single line fitting all the experimental data shows that the inertial regime is independent of the attenuation coefficient.

Thermistor position (mm)	MAX Expt	MAX Calc.	WF Expt	WF Calc.
20	75	95	105	135
85	190	180	220	245
150	260	240	315	320
215	320	295	390	385

TABLE 6. The measured time for the intrusion to reach the thermistor locations for the maximum intensity (MAX) and water filter (WF) experiments is compared with the time calculated from the scaling for the inertial regime. Temperature data were not available for the neutral density filter experiment.

Experiment	Transition time (s) Measured	Transition time (s) Scaling	t/t_E
Maximum	350 ± 50	119	2.9 ± 0.4
'Water' filter	350 ± 50	145	2.4 ± 0.4
Neutral density filter	350 ± 50	131	2.6 ± 0.4

TABLE 7. A comparison between the measured time for the transition to the energy limited regime, and that obtained from the scaling. The ratio t/t_E is also shown.

described fully in Armfield & Patterson (1991), but in brief, finite volumes are used to convert the derivatives to second-order central differences, with the advective terms approximated by the QUICK scheme of Leonard (1979) and the diffusive terms on the irregular grid by the scheme of Patterson (1983). The time integration is carried out by a second-order Crank–Nicholson predictor corrector method. The discretization

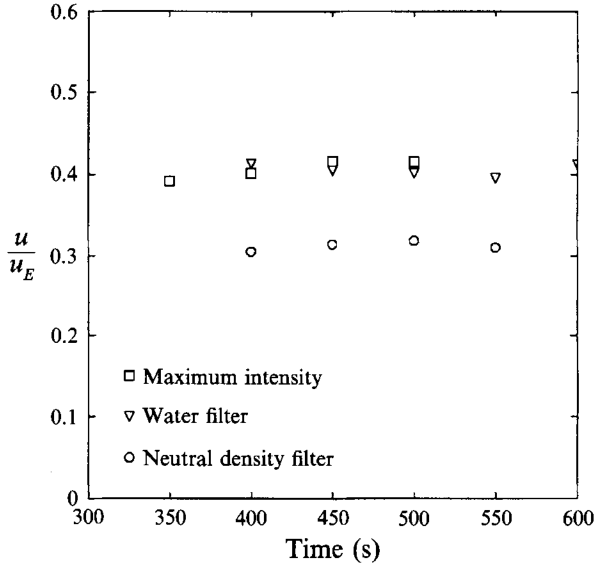

FIGURE 10. The maximum velocity, scaled against the expected constant velocity u_E (equation (25)), plotted against time for the three experiments. The fit to a single value is not good for all experiments. The results suggest that the lamp was not operating at its full intensity for the neutral density filter experiment.

Experiment	Velocity (mm s^{-1}) Measured	Scaling	u/u_E
Maximum	1.0	2.5	0.40
'Water' filter	0.8	2.1	0.38
Neutral density	0.7	2.3	0.30

TABLE 8. A comparison between the measured constant velocity of the energy limited regime and that obtained from the scaling. The ratio u/u_E is also shown.

produces a block tridiagonal matrix, inverted by an ADI method. The method has been fully tested in Armfield & Patterson (1991), and in Coates & Patterson (1992). The numerical code was further tested and verified against the three experiments described in §4. The details of the comparison can also be found in Coates & Patterson (1992).

The non-dimensional scheme used in the numerical simulations was the following:

$$\left.\begin{aligned} &x=\frac{x^*}{h}, \quad z=\frac{z^*}{h}, \quad t=\frac{\nu t^*}{h^2}\left(\frac{Gr}{A_E^2}\right)^{\frac{1}{3}},\\ &u=\frac{hu^*}{\nu(Gr\,A_E)^{\frac{1}{3}}}, \quad w=\frac{hw^*}{\nu(Gr\,A_E)^{\frac{1}{3}}},\\ &T=\frac{g\alpha h^3(T^*-T_0)}{\nu^2(Gr\,A_E)^{\frac{2}{3}}}, \quad F_i=\frac{F_i^*}{F_0},\\ &\eta_i=\eta_i^*\,h, \quad p=\frac{h^2p^*}{\rho_0\,\nu^2}\left(\frac{A_E}{Gr^2}\right)^{\frac{1}{3}}, \end{aligned}\right\} \qquad (33)$$

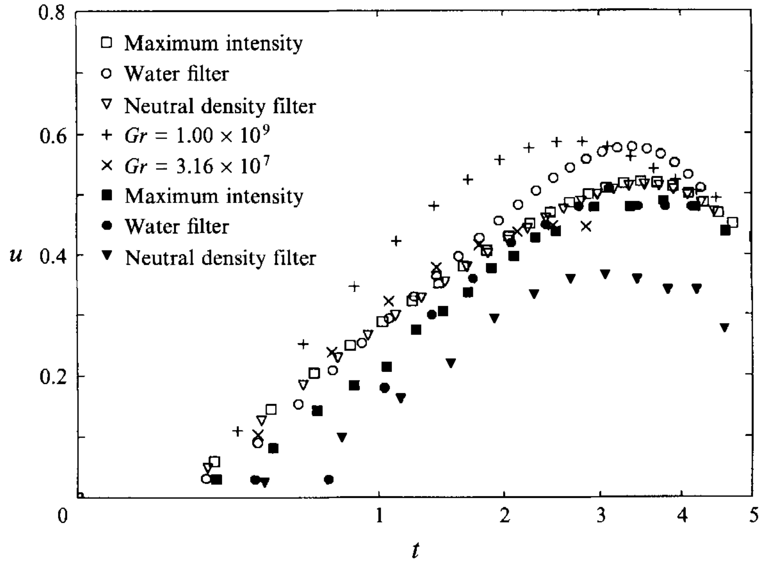

FIGURE 11. The maximum velocity plotted against time for the experiments. The solid symbols are the experiments of §4, non-dimensionalized according to the scheme of §5.1. The open symbols are the numerical simulations of those experiment. The additional numerical experiments are also shown.

where the starred variables are dimensional. These scales arise naturally when the velocities are scaled against the energy-limited intrusion velocity.

With this non-dimensionalization, the scaling relations (18) and (19) reduce to the simple forms

$$u \sim t^{\frac{1}{2}}, \tag{34}$$

$$u_E \sim A_E^{-\frac{2}{3}}, \tag{35}$$

and

$$t_E \sim A_E^{-\frac{4}{3}}. \tag{36}$$

5.2. *Numerical results*

The good agreement between experiment and simulation can be seen in figure 11 in which the dimensionless velocity has been plotted against the square root of the dimensionless time as defined by (33). The experiments described in §4 have been non-dimensionalized with respect to (33), and are plotted as the solid symbols in figure 11. The error bars have been dropped for clarity. The equivalent numerical simulation of each experiment is plotted as the open symbol.

There is a very good match between the slope of the inertial regime for the experiments and their simulations, giving confidence in the numerical code. Similarly, the prediction of the onset of the energy-limited regime and its velocity scale from the simulations is in good agreement for two of the experiments. The numerical simulation of the neutral density experiment is also in good agreement with the rest of the experiments, adding a further weight to the argument that the neutral density experiment may have been run when the lamp was not producing its full intensity.

Two further numerical experiments were run to extend the range of Grashof numbers beyond that available in the laboratory. The values $Gr = 1.00 \times 10^9$ and $Gr = 3.16 \times 10^7$ extend the range to nearly two orders of magnitude. The result of these simulations are also plotted on figure 11. The lower Grashof number experiment is in excellent agreement with the earlier results, showing that the scaling continues to be valid at a Grashof number an order of magnitude lower than that attained in the laboratory. The larger Grashof number case is also in good agreement, with respect to the $t^{\frac{1}{2}}$ dependence and the transition to the energy-limited flow, with a small time offset. Similarly, the velocity scales of the energy-limited regime are also the same for all experiments (other than the neutral density experiment), which provides further confirmation of the scaling relation (25).

6. Conclusions

While a number of scaling regimes for this problem have been found, virtually all typical lakes fall into just one of those regimes. Following a period when the flow is inertial, it will either become viscous or energy limited, depending on the relation between Gr, η_*, and l_E (through A_E). Except for very long and shallow or very turbid lakes, it will be the condition $\eta_*^6 A_E^{-2} < Gr$ that will be satisfied, and the flow regime is the convective regime (*b*) of table 1. It is this condition that is satisfied by the experiments. These have confirmed the validity of this regime, and correctly predict both the inertial and the energy-limited velocity and time scales. The time and velocity scales have been further extended by numerical experiments. These have confirmed their validity over nearly two orders of magnitude. The final transition to the energy-limited–viscous velocity scale (26) predicted by the scaling could not be seen in the experimental results as it would occur long after the interaction of the intrusion with the endwall had distorted the flow and invalidated the scaling (from table 4, $t_v \sim 2000\ s \gg t_T = 600$ s).

This class of flow has importance in natural lakes, as can be seen if we estimate the flow velocities that may occur in small lake with a depth $h = 1$ m, and with an exposed length $l_E = 100$ m. To determine the bulk surface flux and attenuation coefficient, we will assume that the incoming radiation spectrum is a 6000 K black body, with a total energy flux of 640 W m^{-2}, while the water attenuation coefficients over a range of wavebands for clear water are given by Hale & Querry (1973). Fitting a single-band model to these data gives the bulk parameters as $F_0 = 515$ W m^{-2} and $\eta_b = 4.4\ \text{m}^{-1}$, and from (11), the Grashof number is $Gr = 2.4 \times 10^{11}$. The duration of the inertial phase is found from (19) which gives $t_E \sim 3.5 \times 10^3$ s. In the spirit of this estimate, we will assume that the correction factor is the mean of the values t/t_E tabulated in table 7. This gives $t/t_E \approx 2.6$, and 9000 s as the duration of the inertial phase. After this time, the flow becomes energy limited, with a velocity found from (25) of $u_E \sim 29$ mm s^{-1}. Again, the correction factor is assumed to be the mean of the values u/u_E tabulated in table 8, which gives $u/u_E \approx 0.36$, and 9 mm s^{-1} as the estimate for the velocity.

This velocity is quite substantial, acting as it would over many hours. Of course, many other factors are involved in lakes, such as the changing light intensity throughout the day or the presence of the roots of the floating plants extending into the flow, all of which will alter the flow characteristics from the simple model given here. Three-dimensional effects may also influence the result. However, this estimate does serve to show that the differential absorption mechanism may be of importance in the nutrient exchange below a floating plant layer. A better estimate may be made by obtaining improved correction ratios which cover a larger range of values for the parameters. This will be the subject of future research.

It is a pleasure to thank John Taylor and Geoff Schladow for comments on the manuscript, Jörg Imberger for general comments, and John Taylor again and Craig Stevens for their assistance in the laboratory. M. Coates was supported by a University of Western Australia Scholarship and a Centre for Water Research Supplement. This work was partly supported by the Australian Research Council.

REFERENCES

ARMFIELD, S. W. 1991 Finite-difference solutions of the Navier–Stokes equations on staggered and non-staggered grids. *Computers Fluids* **20**, 1–17.

ARMFIELD, S. W. & PATTERSON, J. C. 1991 Direct simulation of wave interactions in unsteady natural convection in a cavity. *Intl J. Heat Mass Transfer* **34**, 929–940.

BECKERMANN, C. & VISKANTA, R. 1988 Natural convection solid/liquid phase change in porous media. *Intl J. Heat Mass Transfer* **31**, 35–46.

BOWMAKER, A. P. 1976 The physico-chemical limnology of the Mwenda River mouth, Lake Kariba. *Arch. Hydrobio.* **77**, 66–108.

CARSLAW, H. S. & JAEGER, J. C. 1978 *Conduction of Heat in Solids*, 2nd edn. Clarendon.

CHELLIAH, S. & VISKANTA, R. 1989 Freezing of water saturated porous media in the presence of natural convection: experiments and analysis. *Trans. ASME C: J. Heat Transfer* **111**, 425–432.

COATES, M. J. 1991 Natural convection due to differential heating from unequal light absorption. PhD thesis, Department of Civil and Environmental Engineering, University of Western Australia.

COATES, M. J. & FERRIS, J. 1992 The radiatively driven natural convection beneath a floating plant layer. *Environmental Dyn. Ref.* ED-581-MC. Centre for Water Research, University of Western Australia.

COATES, M. J. & PATTERSON, J. 1992 Numerical simulation of the natural convection in a cavity with non-uniform internal sources. *Environmental Dyn. Ref.* ED-580-MC. Centre for Water Research, University of Western Australia.

COLLINS, M. J. & EMERY, W. J. 1988 A computational method for estimating sea ice motion in sequential Seasat synthetic aperature radar imagery by matched filtering. *J. Geophys. Res.* **93**, 9241–9251.

FUSEGI, T. & FAROUK, B. 1989 Laminar and turbulent natural convection – radiation interactions in a square enclosure filled with a non-gray gas. *Numer. Heat Transfer* **15**, 303–322.

HALE, G. M. & QUERRY, M. R. 1973 Optical constants of water in the 200 nm to 200 μm wavelength region. *Appl. Optics* **12**, 555–563.

IMBERGER, J. & PATTERSON, J. C. 1990 Physical limnology. *Adv. App. Mech.* **27**, 303–475.

INCROPERA, F. P., CRAIG, T. D. & HOUF, W. G. 1984 Radiation transfer in absorbing and scattering fluids – II. Comparisons of measurements and predictions. *J. Quant. Spect. Radiat. Transfer* **31**, 139–147.

ISLAM, M. R. & NANDAKUMAR, K. 1990 Transient convection in saturated porous layers with internal heat sources. *Intl J. Heat Mass Transfer* **33**, 151–161.

KIRK, J. T. O. 1983 *Light and Photosynthesis in Aquatic Ecosystems*, 1st edn. Cambridge University Press.

KIRK, J. T. O. 1986 Optical limnology – a manifesto. In *Limnology in Australia* (ed. P. De Deckkar & W. D. Williams), pp. 33–62. Published by Dr W. Junk.

LEESE, J. A., NOVAK, C. S. & CLARKE, B. B. 1971 An automated technique for obtaining cloud motion from geosynchronous satellite data using cross correlation. *J. Appl. Met.* **10**, 110–135.

LEONARD, B. P. 1979 A stable and accurate convective modelling procedure based on quadratic upstream interpolation. *Comput. Meth. Appl. Mech. Engng* **19**, 59–98.

NINNIS, R. M., COLLINS, M. J. & EMERY, W. J. 1986 Automated extraction of pack ice motion from advanced very high resolution radiometry imagery. *J. Geophys. Res.* **91**, 10725–10734.

PATTERSON, J. C. 1983 General derivative approximations for finite difference schemes. *Intl J. Numer. Meth. Engng* **19**, 1235–1241.

PATTERSON, J. C. 1984 Unsteady natural convection in a cavity with internal heating and cooling. *J. Fluid Mech.* **140**, 135–151.

PATTERSON, J. C. & IMBERGER, J. 1980 Unsteady natural convection in a rectangular cavity. *J. Fluid Mech.* **100**, 65–86.

SIEGEL, R. & HOWELL, J. R. 1981 *Thermal Radiation Heat Transfer*, 2nd edn. Hemisphere.

SOUFIANI, A. & TAINE, J. 1987 Application of statistical narrow-band model to coupled radiation and convection at high temperature. *Intl J. Heat Mass Transfer* **30**, 437–447.

STEVENS, C. L. & COATES, M. J. 1993 A maximized cross correlation technique for resolving velocity fields in laboratory experiments. *IAHR J. Hydraulic Res.* (in press).

TREVISAN, O. V. & BEJAN, A. 1986 Convection driven by the nonuniform absorption of thermal radiation at the free surface of a stagnant pool. *Numer. Heat Transfer* **10**, 483–506 (referred to herein as TB).

VISKANTA, R. & TOOR, J. S. 1978 Absorption of solar radiation in ponds. *Solar Energy* **21**, 17–25.

WEBB, B. W. & VISKANTA, R. 1987 Radiation-induced buoyancy-driven flow in rectangular enclosures: experiment and analysis. *Trans. ASME* C: *J. Heat Transfer* **109**, 427–433.

ZOHARY, T. & MADEIRA, A. M. P. 1990 Structural, physical and chemical characteristics of *Microcystis aeruginosa* hyperscums from a hypertrophic lake. *Fresh Water Biol.* **23**, 339–352.